ACS OMEGA

http://pubs.acs.org/journal/acsodf

Article

Effect of Precursor Status on the Transition from Complex to Carbon Shell in a Platinum Core−Carbon Shell Catalyst

Jihyeok Song,[‖] Youngkwang Kim,[‖] Hyo Eun Bae, Sun Young Kang, Jongmin Lee, Mohanraju Karuppannan, Yung-Eun Sung, Yong-Hun Cho,* and Oh Joong Kwon*

Cite This: *ACS Omega* 2022, 7, 15615−15624

Read Online

ACCESS | Metrics & More | Article Recommendations | Supporting Information

ABSTRACT: Encapsulating platinum nanoparticles with a carbon shell can increase the stability of core platinum nanoparticles by preventing their dissolution and agglomeration. In this study, the synthesis mechanism of a platinum core−carbon shell catalyst via thermal reduction of a platinum−aniline complex was investigated to determine how the carbon shell forms and identify the key factor determining the properties of the Pt core−carbon shell catalyst. Three catalysts originating from the complexes with different platinum to carbon precursor ratios were synthesized through pyrolysis. Their structural characteristics were examined using various analysis techniques, and their electrochemical activity and stability were evaluated through half-cell and unit-cell tests. The relationship between the nitrogen to platinum ratio and structural characteristics was revealed, and the effects on the electrochemical activity and stability were discussed. The ratio of the carbon precursor to platinum was the decisive factor determining the properties of the platinum core−carbon shell catalyst.

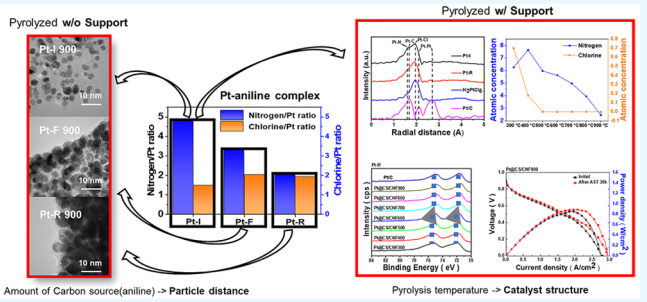

1. INTRODUCTION

Nanoparticle-based electrochemical catalysts have been studied for their application in fuel cells while attempting to improve their activity.[1−14] Many studies have been conducted worldwide over the past decade that have greatly improved the activity of oxygen reduction catalysts. However, their durability remains a great limiter of their commercialization despite the enhancement in activity. When Pt nanoparticles are applied as electrochemical catalysts in fuel cells, they are oxidized, dissolved, and agglomerated, reducing their surface area,[1,8,15−24] which leads to low catalytic activity and a decrease in performance. This occurs more easily when the nanoparticles are smaller. Among the various methods for resolving this issue, encasing the metal nanoparticles in a carbon shell is not only effective for improving durability of electrochemical catalyst, but also as an upscaling process.[18] The applicability of carbon shell protective layer in heterogeneous catalysis and photocatalysis has also been investigated in this regard.[25]

If the platinum nanoparticles can be individually encased within an electrochemically stable protective layer, their stability can be improved. Silicon dioxide, magnesium oxide, and graphitic carbon, which are chemically stable under fuel cell driving conditions, can prevent platinum nanoparticles from dissolving, Ostwald ripening, and aggregation.[26−43] Carbon is the best protective layer material as gaseous substances, such as oxygen, can easily pass through it.[28−34,37−44] The process of carbon shell formation on platinum nanoparticles generally consists of three steps: platinum nanoparticle synthesis, carbon precursor layer formation on the nanoparticles, and subsequent carbonization. For example, Tong et al. synthesized platinum nanoparticles on a carbon nanotube and formed a glucose-containing polymer layer, a carbon precursor, on them. A carbon shell was formed by carbonizing the glucose through heat treatment.[21] Nie et al. formed a polyaniline layer on Pt/C through oxidative polymerization of aniline monomer with ammonium peroxydisulfate. The formed polymer layer was heat-treated at 900 °C to form a carbon shell, which effectively prevented the dissolution and aggregation of platinum.[23] In the processes, monomers, such as aniline, glucose, and dopamine are typically introduced to coat the metal nanoparticles with a polymer layer. If the polymer layer is too thick, the oxygen permeability decreases significantly, and the stability of the nanoparticle decreases after pyrolysis if it is too thin.[18−21,37] For fine carbon encapsulation, it is important to form a polymer layer with a controlled thickness and uniform coating. However, it is very difficult to uniformly coat nanometer-sized metal particles with a subnanometer-sized polymer layer.

Received: January 20, 2022
Accepted: April 13, 2022
Published: April 27, 2022

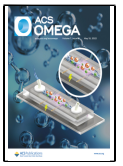

Scheme 1. Synthesis Scheme of Three Pt−Aniline Complexes (Pt-I, Pt-F, and Pt-R)

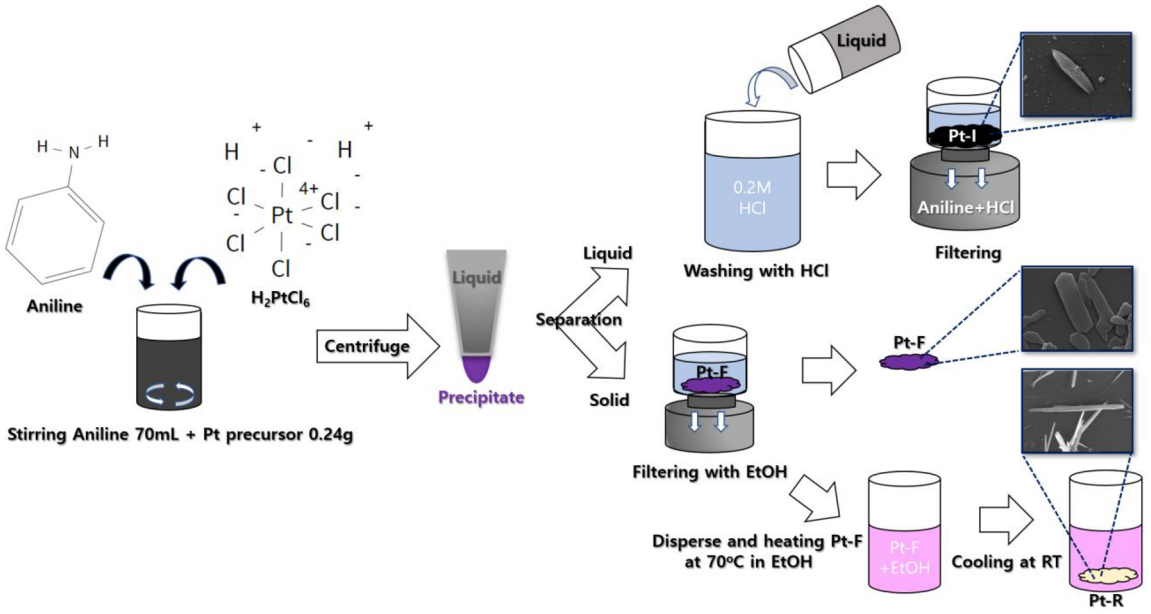

Recently, new attempts have been made to form carbon shells on platinum nanoparticles using platinum and aniline complexes,[8,18,37] which are pyrolyzed to thermally reduce platinum and carbonize the aniline monomer simultaneously, thus synthesizing platinum nanoparticles encased in a carbon shell. Although the complex can be pyrolyzed at a high temperature, the platinum nanoparticles can maintain a small size with uniform distribution owing to the carbon shell with a uniform thickness of less than 1 nm. The thickness of the carbon shell can be made uniform by fixing the ratio of platinum ions to the aniline monomer. This approach opens up new possibilities for easily producing metal nanoparticles with a more uniform carbon shell than conventional methods.[18]

The method using a Pt−aniline complex provides new insight for encasing platinum nanoparticles with carbon shells; however, the process is not yet clearly understood, and the effect of the ratio of platinum to carbon source remains unclear. In this study, we attempted to elucidate how the platinum−aniline complex decomposes when heat-treated at different temperatures to evaluate the reduction of platinum ions and carbonization of aniline. Furthermore, the structural characteristics of the Pt core−carbon shell catalyst depending on the structure of the platinum−aniline complex and the Pt to carbon ratio were studied based on three kinds of complexes. The original structure and structural change of the Pt−aniline complex according to the pyrolysis temperature are suggested, and the correlation between the electrochemical activity and the complex structure is explained using half-cell and unit-cell tests.

2. EXPERIMENTAL SECTION

2.1. Pt−Aniline Complex Preparation. Briefly, 0.24 g of Pt precursor ($H_2PtCl_6{\cdot}6H_2O$) and 70 mL of aniline were mixed and stirred for 5 h to form a platinum−aniline complex solution, which was then centrifuged at 10,000 rpm for 30 min. A purple precipitate was obtained and denoted as Pt-F (platinum-final product). The solution was separately collected and further treated by mixing with an aqueous 0.2 M HCl solution to remove additional aniline. The mixture was filtered and rinsed with deionized (DI) water, and the powder remaining on the filter paper was denoted as Pt-I (platinum-intermediate). Both the Pt-F and Pt-I were dried in an oven at 70 °C for 1 h. For the recrystallization of Pt-F, the Pt-F powder was dispersed in ethanol and the temperature of the solution was increased to 70 °C. When a white precipitate appeared, the solution was cooled slowly and filtered at room temperature. The recrystallized Pt-F was denoted as Pt-R (platinum-recrystallized). The simplified process is shown in Scheme 1, and the detailed Pt-I preparation process is provided in our previous study.[18]

2.2. Pt Core−Carbon Shell Electrocatalyst Synthesis. To investigate the encapsulation characteristics of the complexes, the Pt-I, Pt-F, and Pt-R were heat-treated at 900 °C without support and denoted as Pt-I900, Pt-F900, and Pt-R900, respectively. Additionally, to explore encapsulation on a support, Pt core-carbon shell electrocatalysts were also synthesized on carbon nanofibers (CNFs) by Pt-I, Pt-F, and Pt-R loading. CNFs were dispersed in ethanol for 30 min using a sonic bath. When the dispersion was complete, the Pt-I, Pt-F, and Pt-R complexes were added to the solution at a ratio of 1:1.2 and were dispersed for an additional 3 min. Pt-I, Pt-F, and Pt-R-loaded CNFs (Pt-I/CNF, Pt-F/CNF, and Pt-R/CNF, respectively) were obtained by drying the ethanol at 70 °C using a rotary evaporator. The Pt-I, Pt-F, and Pt-R/CNFs were then pyrolyzed at 900 °C at a heating rate of 3 °C min^{-1} under a nitrogen atmosphere using a tube furnace. The catalysts were denoted as Pt-I@CS/CNF900, Pt-F@CS/CNF900, and Pt-R@CS/CNF900, respectively. Weight percentages of Pt-I@CS/CNF900, Pt-F@CS/CNF900, and Pt-R@CS/CNF900 which was calculated by inductively coupled plasma-atomic emission spectroscopy (ICP-AES; PerkinElmer, Optima-4300 DV, USA) result were 26.5%, 23.9%, 34.5% respectively. To examine the structural change in relation to the pyrolysis temperature, Pt-I on CNF was pyrolyzed at temperatures of 300, 400, 500, 600, 700, and 800 °C under the same conditions used for Pt-I on CNF pyrolysis, excluding the temperature. Based on the heat treatment temperature, the samples were denoted as Pt@CS/CNF300,

https://doi.org/10.1021/acsomega.2c00418
ACS Omega 2022, 7, 15615−15624

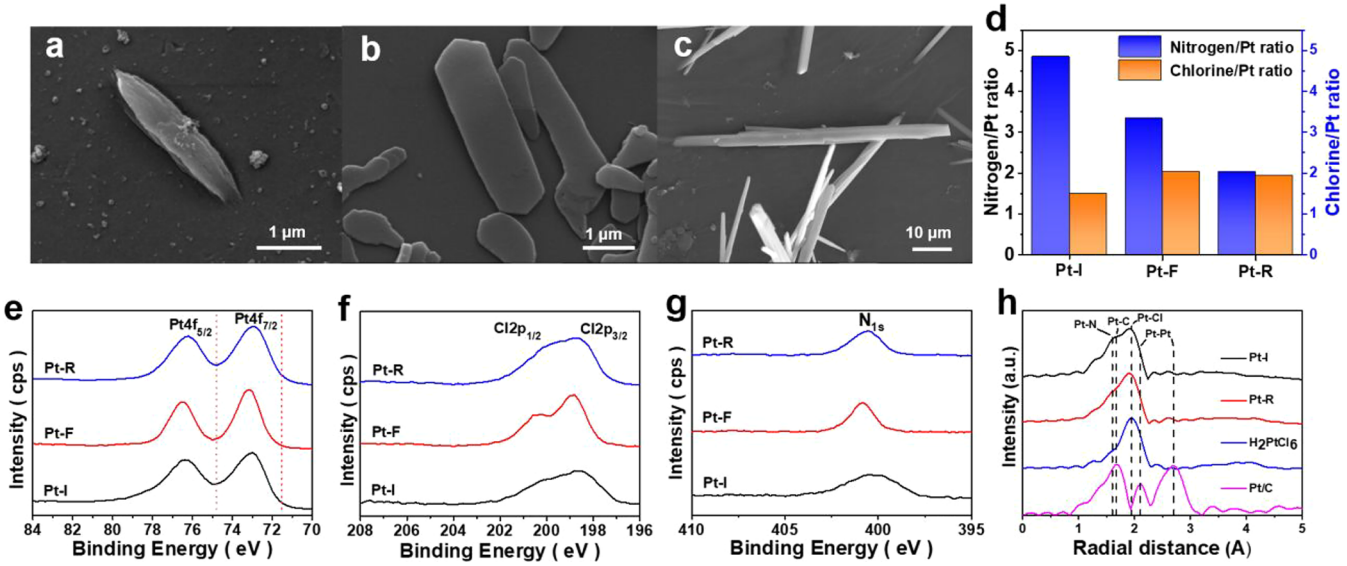

Figure 1. SEM images of (a) Pt-I, (b) Pt-F, and (c) Pt-R. (d) Atomic ratio of nitrogen and chlorine to platinum. XPS spectra of (e) Pt 4f, (f) Cl 2p, and (g) N 1s. (h) EXAFS spectra of Pt-I, Pt-R, H_2PtCl_6, and Pt/C.

Pt@CS/CNF400, Pt@CS/CNF500, Pt@CS/CNF600, Pt@CS/CNF700, and Pt@CS/CNF800, respectively.

2.3. Characterization. A scanning electron microscope (FE-SEM; EDS-7800F, JEOL, Japan) and high-resolution transmission electron microscope (HR-TEM; Talos F200X, FEI, USA) were used to investigate the surface morphology of the platinum nanoparticles and carbon shells. An X-ray diffractometer (Smart Lab, Rigaku, Japan) was used to investigate the crystal structures and crystallite size of the catalyst with Cu Kα radiation (1.54 Å) as a light source. The crystallite size was calculated using Scherrer's equation of $L_{hkl} = K\lambda/B_{hkl} \cos\theta$, where L_{hkl} stands for average crystallite size, K is the numerical factor being dependent on crystallite shape, which is 0.9 in the absence of detailed shape information, λ is the wavelength of the X-ray, B_{hkl} is the full-width at half-maximum of the peak, and θ is the Bragg angle of each diffraction peak. Thermogravimetric analysis (TGA; TGA N-1000/1500, SCINCO, Republic of Korea) was conducted to observe the structure and decomposition of the complexes. The platinum chemical states were confirmed using an X-ray photoelectron spectrometer (XPS; PHI 5000 Versa Probe II, ULVAC-PHI, Japan) and an extended X-ray absorption fine structure (EXAFS; 10C beamline of Pohang Accelerator Laboratory (PAL), Republic of Korea).

2.4. Half-Cell Tests. Half-cell experiments were conducted using a three-electrode system. A glassy carbon electrode (0.196 cm^2) connected to a rotating disk electrode (RDE) and a graphite bar were used as the working electrode and the counter electrode, respectively, and an Ag/AgCl single-junction electrode was used as the reference electrode. The potential was reported in reference to a reversible hydrogen electrode (RHE) by calibrating the Ag/AgCl single-junction electrode in 0.1 M $HClO_4$ solution before each experiment. The electrochemical experiment was conducted by connecting the three-electrode system to a potentiostat device (NOVA, Autolab).

For the half-cell test, a catalyst ink was prepared by adding the synthesized catalysts, an ionomer (Nafion solution 5 wt %, CNL), and ethanol to a vial and dispersing the solution under ultrasonication for 30 min. Upon completing dispersion, 10 μg_{Pt} cm^{-2} of the catalysts was placed on a glassy carbon electrode and dried. After setting the three-electrode system, cyclic voltammetry (CV) and linear sweep voltammetry (LSV) were conducted to confirm the activity of the catalyst. Argon gas was purged into the electrolyte before CV measurement, and potential was then applied at a rate of 500 mV s^{-1} in the range of 0.05−1.2 V (vs RHE) to activate the catalyst. To calculate the electrochemical surface area (ECSA), a voltage was applied at a rate of 100 mV s^{-1} in the range of 0.05−1.0 V (vs RHE). LSV was conducted to evaluate the activity of the catalyst in the oxygen reduction reaction (ORR). Before measurement, oxygen was purged into the electrolyte to saturate it. The experiment commenced after rotating the RDE at 1,600 rpm. In the LSV measurement experiment, potential was applied in the positive scan direction at a scanning rate of 20 mV s^{-1} in a potential range of 0.05 to 1.05 V (vs RHE).

2.5. Unit-Cell Test. The membrane electrode assembly (MEA) was fabricated following a catalyst-coated membrane method by using 0.1 mg_{Pt} cm^{-2} of the synthesized catalysts as the cathode and 0.025 mg_{Pt} cm^{-2} of Pt/C (40 wt %, Johnson Matthey) as the anode. Nafion 212 (Dupont) and carbon paper (SIGRACET, GDL 39BC) were introduced to the membrane and gas diffusion layer (GDL), respectively. The anode catalyst ink was prepared by dispersing 3 mg of Pt/C and 21.6 μL of Nafion solution in 600 μL of isopropyl alcohol (IPA) in a vial using a sonicator. The catalyst ink for the cathode was prepared using 10 mg of the synthesized catalyst, 1 mL of *N*-propyl alcohol (NPA), and 84 μL of Nafion solution. After coating the catalyst inks on each side of the membrane, the MEA was sandwiched between the GDLs. A fuel cell test station (CNL Energy, Seoul, Republic of Korea) was used to obtain the polarization curve. Before obtaining the polarization curve, the catalyst was activated by providing H_2 (100 ccm) to the anode and N_2 (50 ccm) to the cathode and cycling the voltage between 0.05 and 1.2 V at a scan rate of 100 mV s^{-1}. To examine the performance, humidified H_2 and air were supplied to the anode and cathode at flow rates of 350 and 1600 ccm, respectively. To test the durability of the MEA, 30 000 square wave cycles of potential were repeated between 0.6 and 0.95 V.

https://doi.org/10.1021/acsomega.2c00418
ACS Omega 2022, 7, 15615−15624

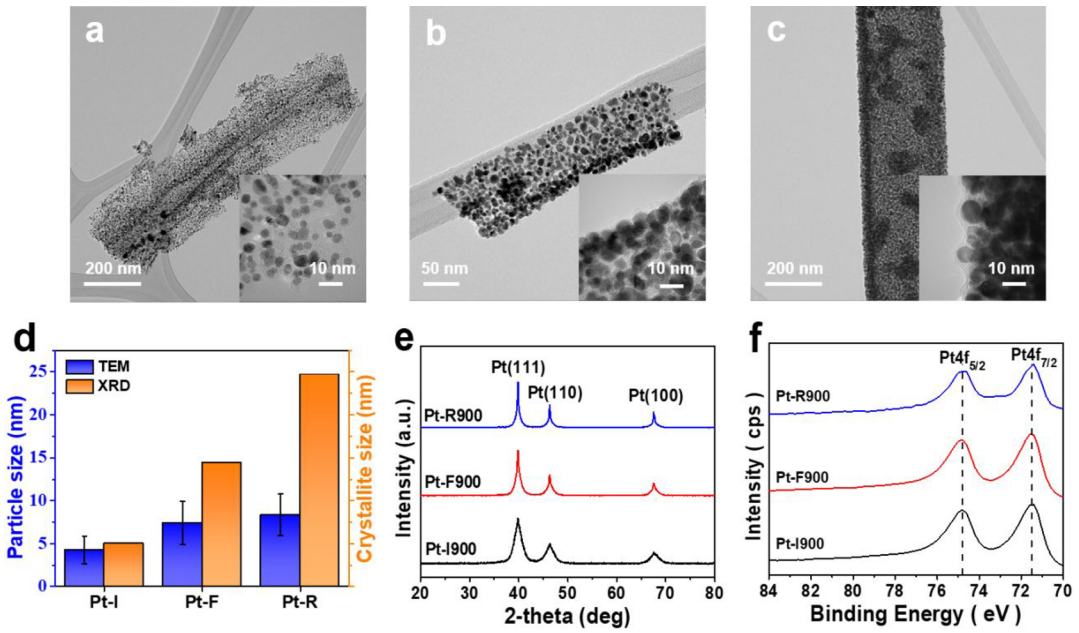

Figure 2. HR-TEM images of (a) Pt-I, (b) Pt-F, and (c) Pt-R pyrolyzed w/o CNF. (d) Mean particle size obtained from TEM and XRD data. (e) XRD patterns and (f) XPS spectra of Pt-I, Pt-F, and Pt-R pyrolyzed w/o CNF.

3. RESULTS AND DISCUSSION

3.1. Structure of the Platinum−Aniline Complex. To determine the shapes of the three platinum−aniline complex powders, each sample was observed using a SEM (Figure 1a−c). The Pt-I complex was shaped similarly to a pointed rugby ball, while Pt-F had a long, hexagonal-shaped plate. The Pt-R obtained by removing excess aniline monomer from Pt-F with ethanol exhibited a long needle shape (Figure 1c). According to the atomic ratios calculated from the XPS (Figure S1), the atomic ratio of nitrogen to platinum in Pt-F, corresponding to the relative amount of aniline to platinum in the complex, was smaller than that of Pt-I, while the relative ratio of chlorine increased (Figure 1d). The nitrogen to platinum ratio of Pt-R was lowest among the three samples; however, the chlorine ratio between Pt-F and Pt-R was fixed at 2. This indicates that additional ethanol washing only removed the excess aniline monomer and not the aniline or chlorine bonded to platinum in the complex. Aniline removal could be confirmed by the TGA analysis shown in Figure S2a. Weight loss around 150 °C related to aniline evaporation disappeared in the Pt-R, but was observed in the Pt-F. The platinum:aniline:chlorine ratios of Pt-I, Pt-F, and Pt-R were 1:4.8:1.5, 1:3.3:2, and 1:2:1.9, respectively. From the decrease in the N/Pt ratio, it can be inferred that the Pt-I with a high N/Pt ratio of 4.8 transforms into Pt-R (trans-Pt(aniline)$_2$Cl$_2$) with an N/Pt ratio of 2 over time. When preparing the three complexes, the relative amount of Pt-F to Pt-I increased with increasing preparation time (Scheme 1). The atomic ratio of Pt-R, which was purified from Pt-F by removing excess aniline, was also supported by the TGA data shown in Figure S2b. By dividing the weight loss detected at each stage by the molecular weight of the related molecule, the relative atomic ratio was determined to be 1:2.1:1.64.

The crystalline structure of the complex powder and chemical status of the elements were explored by XRD (Figure S3), XPS (Figure 1e−g), and EXAFS (Figure 1h). From XRD data in Figure S3, it can be known that the peaks locating between 20 and 30 come from aniline−HCl and Pt−N.[45] Pt-I has strong peaks in both the red and blue regions while Pt-R has definite peak in the red region. Pt-F only has strong intensity in the blue region. It can be inferred that three complexes have different crystalline structure from XRD pattern. In the XPS, the three Pt−aniline complexes exhibited peaks related to Pt 4f, N 1s, and Cl 2p. The complexes showed higher binding energies for the Pt $4f_{7/2}$ (73 eV for Pt-I, 73.2 eV for Pt-F, and 73 eV for Pt-R) and $4f_{5/2}$ (76.4 eV for Pt-I, 76.5 eV for Pt-F, and 76.3 eV for Pt-R, respectively) peaks than those of metallic platinum (71.5 eV for Pt $4f_{7/2}$ and 74.8 eV for Pt $4f_{5/2}$). It is difficult to identify exact peaks in the literature or reported papers that match the observed peaks, but we can know that the peaks are related to the chemicals that consist of platinum, nitrogen, and chlorine from the National Institute of Standards and Technology (NIST, U.S. Department of Commerce) XPS database. The N 1s peak indicates that Pt and N formed a complex by presenting a N 1s peak with a binding energy higher than that appearing at 399.40 eV for aniline. Pt-F and Pt-R exhibited similar shapes for Cl $2p_{1/2}$, Cl $2P_{3/2}$, and N 1s, while Pt-I exhibited broad peaks that were slightly shifted to lower binding energies. This indicates that the structure of Pt-I differed to those of Pt-F and Pt-R. EXAFS provides important information regarding the structures of the three complexes. Pt−Pt contributions at 2.7 and 2.09 Å were absent in the k^3-weighted Fourier transform of EXAFS at the Pt L_3 edge for Pt-I, Pt-F, and Pt-R, which strongly indicates that Pt did not exist in the metallic state in the three complexes. On the other hand, prominent shells located at 1.93 and 1.59 Å arose from Pt−Cl and Pt−N, respectively, in Pt-I, Pt-F, and Pt-R demonstrating that nitrogen and chlorine form complexes with platinum. The relative intensity of Pt−N in the three complexes is consistent with the N:Pt ratio obtained from XPS.

To investigate how the structure and composition of the complexes affected the encapsulation of platinum with a carbon shell, the complexes were pyrolyzed at a high temperature of 900 °C without support. The TEM images in

https://doi.org/10.1021/acsomega.2c00418
ACS Omega 2022, 7, 15615−15624

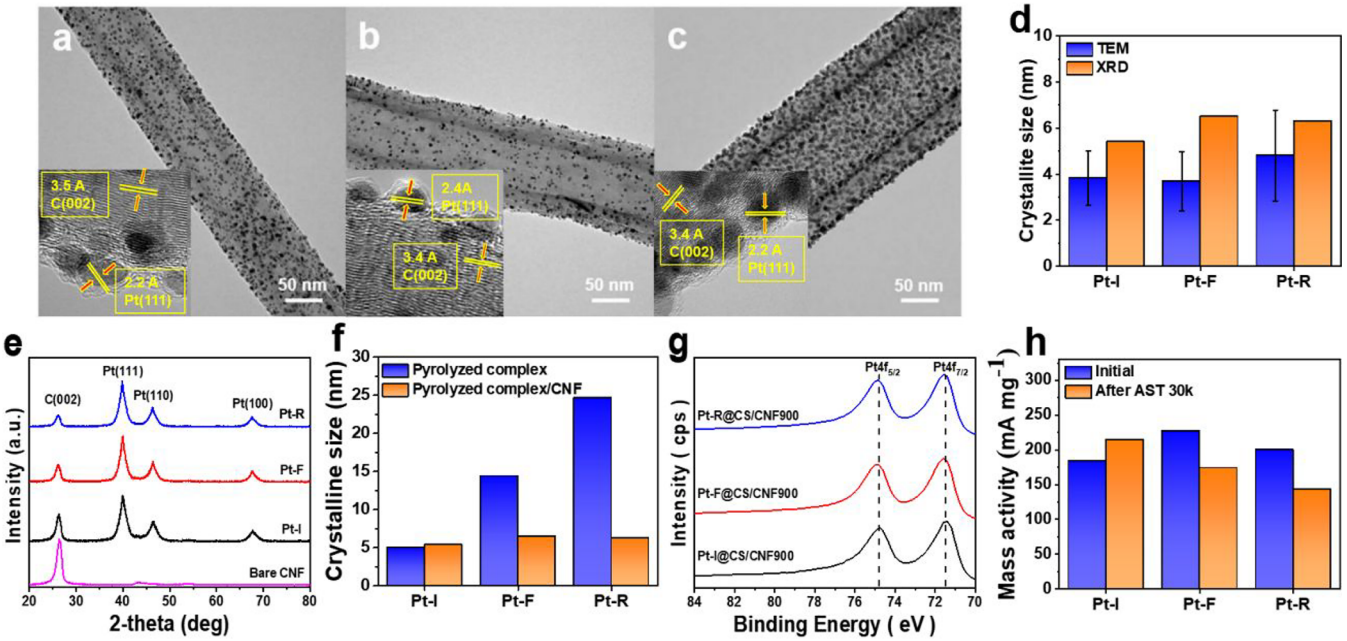

Figure 3. HR-TEM images of (a) Pt-I, (b) Pt-F, and (c) Pt-R pyrolyzed on the CNF. (d) Mean particle size measured from TEM and calculated by Scherrer equation with (e) XRD patterns. (f) Crystalline size comparison depending on the presence of CNFs. (g) XPS spectra and (h) mass activity calculated from half-cell results of pyrolyzed Pt-I, Pt-F, and Pt-R w/CNF.

Figures 2a–c and S4 reveal the effect of the complex status on the structure of the platinum encased in the carbon layer. The size of the platinum particles was inversely proportional to the nitrogen to platinum ratio in the complex, with mean sizes of 4.28, 7.41, and 8.36 nm for Pt-I, Pt-F, and Pt-R, respectively (Figure S5). However, the density of particles was lower in the complex with a high nitrogen to platinum ratio, as shown in the inset images in Figure 2a–c. Furthermore, the distance between particles was large in Pt-I, while the platinum particles in Pt-F and Pt-R aggregated with one another, to an extent. The increase in the particle size and aggregation of Pt nanoparticles in Pt-F and Pt-R were also supported by the mean crystallite size calculated from XRD (Figure 2, parts d and e). The XRD results exhibited a more dramatic increase in the crystallite size than that measured by TEM, as the XRD data can reflect the aggregation of particles by average value, while the size obtained from TEM was measured manually. The TEM and XRD data suggest that the growth of platinum nanoparticles could be effectively inhibited by aniline (i.e., carbon shell after the carbonization of aniline) at a high aniline-to-platinum ratio during pyrolysis, as the amount of aniline was sufficient to maintain the distance between particles. Additionally, the status of aniline in Pt-I, Pt-F, and Pt-R affected its role. When aniline was present as a complex with platinum, such as Pt-I, the aggregation of platinum particles was successfully prevented during pyrolysis; however, aggregation occurred in the Pt-F, in which extra aniline was simply mixed with Pt-R, despite the high nitrogen (i.e., aniline) to platinum ratio. The status of platinum was independent of the status of aniline, as it exhibited the same peak position as metallic platinum (74.8 eV for Pt $4f_{5/2}$ and 71.5 eV for Pt $4f_{7/2}$) after pyrolysis, as shown in Figure 2f. In particular, the peak shift observed in Figure 1e disappeared due to the decomposition of the complex at high temperature.

To obtain a highly exposed electrochemical surface area, the complexes were loaded onto CNFs and pyrolyzed at 900 °C. The largest dissimilarity between the platinum nanoparticles encapsulated by the carbon shell on CNF and without CNF was taken as the mean particle size and distribution of nanoparticles. Unlike the size and distribution shown in Figure 2a-d, Pt-I, Pt-F, and Pt-R had comparable particle sizes of 3.8, 3.7, and 4.8 nm on CNF, respectively, as shown in the TEM images in Figures 3a–c and S6. The XRD data also revealed that the nanoparticles had similar crystallite size on CNF (Figures 3, parts d and e). The small size was achievable because the complexes evenly covering the CNFs were anchored to them by the interaction between the aniline and CNF. Therefore, they exhibited different sizes depending on the presence of CNFs, as shown in Figure 3f. The same XPS data of metallic platinum were observed on the CNF as the XPS data reported without CNF in Figure 3g. The metallic status of platinum is not affected by the existence of support. Additionally, nitrogen and chlorine exhibited similar peak spectra, as shown in Figure S7, regardless of the presence of CNF.

The effect of carbon shells originating from different complexes on the electrochemical activity and stability of the platinum core metal was examined via the LSV test of the oxygen reduction reaction, and the results are shown in Figures 3h and Figure S8. The three samples exhibited different activities and stabilities. Following the accelerated durability test (ADT) for 30k cycles, Pt-I@CS/CNF showed an improved mass activity, while the other samples exhibited degradation in stability, resulting in reduced mass activity and ECSA but increased particle size. It was confirmed that Pt-I@CS/CNF can retain its ECSA better than Pt-F and Pt-R do as shown in Figure S9, obtained from CV test before and after ADT 30k cycles. In addition, TEM analysis performed after ADT showed slight increase in particle size for Pt-F and Pt-R (Figure S10). The carbon shells derived from Pt-F and Pt-R were composed of a lower weight percentage than that originating from Pt-I, as shown in the TGA data provided in

https://doi.org/10.1021/acsomega.2c00418
ACS Omega 2022, 7, 15615−15624

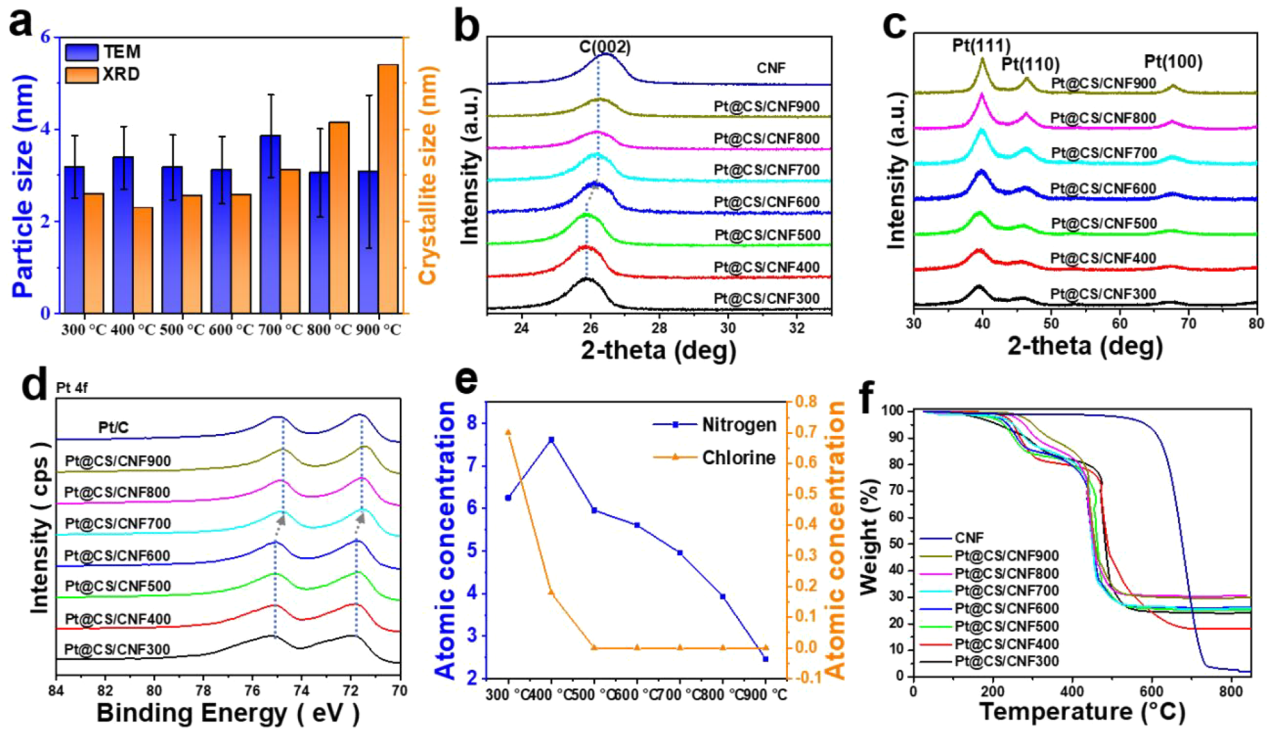

Figure 4. (a) Particle size distribution measured from TEM and calculated by the Scherrer equation. (b) C(002) peak and (c) Pt(111), Pt(110), and Pt(100) peaks observed in the XRD spectra. (d) XPS spectra of Pt 4f, (e) atomic concentration of nitrogen and chlorine, and (f) TGA profile of Pt@CS/CNF 300−900.

Figure S2d, despite the similar thicknesses of the three samples, as shown in the insets of Figure 3a−c. From this, it can be assumed that Pt-I@CS/CNF had a denser carbon shell than the others; thus, it more effectively prevented the dissolution of platinum, enhancing the catalyst stability. The high aniline-to-platinum ratio of Pt-I may have resulted in such carbon layer characteristics.

3.2. Transition from the Complex to the Carbon Layer-Coated Platinum. Pt-I with a sufficient aniline content and fixed proximity to platinum was the most suitable complex among the three studied for encapsulating Pt nanoparticles with carbon shells. When Pt-I is pyrolyzed, platinum ions are reduced and anilines are carbonized; thus, they transform into a platinum core-carbon shell catalyst. However, the transition during heat treatment has not yet been clearly analyzed. To determine how Pt-I is decomposed and a carbon shell is formed, the structure of Pt@CS/CNF originating from Pt-I was investigated after pyrolyzing the Pt-I on CNFs at various temperatures. All samples had a carbon layer on each particle, regardless of the pyrolysis temperature, and the size of the nanoparticles was approximately 3 nm (Figures 4a and S11). The carbon shell formed as an uneven layer up to 500 °C, but it was graphitized when pyrolyzed at temperatures exceeding 600 °C, as shown in Figures S12 and S13. The C(002) of CNF exhibited a peak at 26.4°, while there was a peak at 25.8° for Pt@CS/CNF300−500 and 26.1° for Pt@CS/CNF600−900 (Figure 4b). The C(002) peak appeared at a lower angle than that of CNF at Pt@CS/CNF300−500; however, the peak shifted closer to CNF as the pyrolysis temperature increased. This is because Pt-I was not completely decomposed up to 500 °C, and aniline interacted with CNF; thus, it exhibited different characteristics to CNF. However, the carbon shell became graphitic close to CNF, as it was pyrolyzed at temperatures higher than 600 °C. Raman data (Figure S14) support that the carbon shell become graphitic as the pyrolysis temperature increases. This result is consistent with the decomposition temperature of the complexes, as verified by TGA (Figure S2a).

The crystallite size obtained from XRD (Figure 4c) and the particle size measured at TEM are summarized in Figure 4a and Table S1, and are also provided in Figure S11. The crystallite size was 2.5 nm from 300 to 600 °C, but began to increase to 3.1 nm at 700 °C, and reached 4.14 and 5.39 nm at 800 and 900 °C, respectively, according to the XRD data. However, the TEM results showed a similar size of approximately 3 nm, independent from the pyrolysis temperature, excluding the large deviation at 900 °C. The mismatch between crystallite size and particle size was due to the different platinum statuses. When Pt-I was not completely decomposed below 600 °C, platinum exists in a state bonded with aniline via nitrogen, while chlorine decomposed. Chlorine in Pt-I fragmented between 250 and 450 °C, as it did in Pt-R (Figure S2a).[46] Subsequently, platinum coexisted with aniline until 600 °C. Thus, the crystallite size derived from XRD was smaller than that measured by TEM, which displayed the overall size at low temperatures. As the pyrolysis temperature was raised, the single crystal ratio increased as aniline carbonized, leaving carbon and nitrogen floating on the surface.[47,48] Therefore, the crystal size of Pt@CS/CNF900 was larger than that measured by TEM due to high single crystallinity at high temperature.[49] The Pt(111) peaks of Pt@CS/CNF300−500, Pt@CS/CNF600−800, and Pt@CS/CNF900 were observed at 39.41°, 39.8°, and 40°, respectively (Figure 4c). The Pt(111) peak approached the peak of bulk platinum in accordance with the pyrolysis temperature.

https://doi.org/10.1021/acsomega.2c00418
ACS Omega 2022, 7, 15615−15624

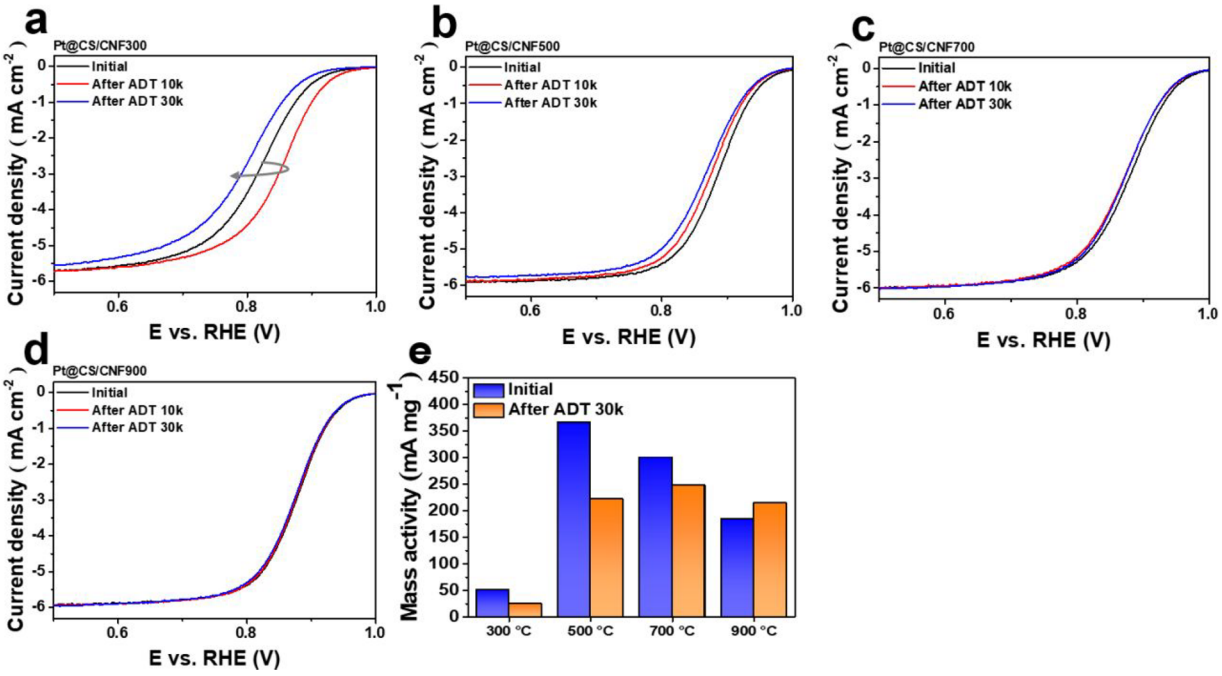

Figure 5. ORR polarization curves of Pt@CS/CNF pyrolyzed at (a) 300, (b) 500, (c) 700, and (d) 900. (e) Mass activity of Pt@CS/CNF300, 500, 700, and 900 before and after ADT 30k cycles.

The chemical state of Pt was investigated by analyzing the binding energy of Pt 4f of Pt@CS/CNFs using XPS (Figures 4d and S15 for C 1s, N 1s, O 1s, and Cl 2p). The binding energy of each Pt $4f_{5/2}$ peak was 75.21, 75.10, 75.10, 75.08, 74.86, 74.90, and 74.80 eV for Pt@CS/CNF300, 400, 500, 600, 700, 800, and 900, respectively. Similarly, the binding energies of the Pt $4f_{7/2}$ peaks were 71.89, 71.85, 71.75, 71.76, 71.55, 71.56, and 71.46 eV, respectively. The XPS results indicate that Pt approached a metallic state as chlorine and aniline decomposed in accordance with the pyrolysis temperature. Figure 4e and Table S2 show the variations in the atomic concentrations of chlorine and nitrogen in relation to the pyrolysis temperature. Chlorine was detected up to 400 °C and disappeared at temperatures above 500 °C. Nitrogen maintained a similar atomic concentration between 300 and 400 °C; however, it began to decrease after 500 °C and linearly decreased to 2.46% until 900 °C. As the carbon shell lost nitrogen and became graphitic according to the pyrolysis temperature, it became more robust, as indicated by the weight loss between 200 and 400 °C in the TGA presented in Figure 4f. The carbon shell of Pt@CS/CNF900 degraded at the highest temperature. Thus, it can be deduced that Pt@CS/CNF900 had the strongest carbon shell.

The TGA, TEM, XRD, and XPS analyses revealed the mechanism of the Pt-I complex transformed into the platinum core−carbon shell. As the temperature increased during pyrolysis, chlorine was removed from the complex first (TGA and XPS). Then, aniline complexed with Pt in Pt-I began to decompose at temperatures exceeding 400 °C, and the decomposition completed at approximately 600 °C leaving carbon and nitrogen (TGA and XPS). Owing to the coexistence of platinum and aniline below 600 °C, the XRD exhibited a smaller crystallite size than the particle size measured by TEM. However, the single crystalline ratio increased at temperatures above 600 °C due to the decomposition of aniline; thus, the XRD results suggested a larger crystalline size than the particle size measured by the TEM results. Additionally, platinum became metallic at temperatures above 600 °C, as indicated by the XPS results.

The atomic concentration of nitrogen did not greatly change up to 600 °C. Nitrogen is a link mediator between CNF and aniline,[50] and it was also connected to platinum in the complex; thus, platinum maintained a small size up to 600 °C due to the connection between carbon, nitrogen, and platinum, preventing agglomeration. Above 600 °C, when the amount of nitrogen began to decrease, the carbon layer acted as a barrier hindering agglomeration, thus maintaining a small particle size, even at 900 °C. After the completion of aniline decomposition and the beginning of nitrogen reduction, the carbon shell became graphitic (XRD and TEM). Thus, the carbon shell prepared at 900 °C was the most robust (TGA).

3.3. Carbon Shell Effect on Electrochemical Activity and Stability. Among the synthesized catalysts, the activity and stability of Pt@CS/CNF300, Pt@CS/CNF500, Pt@CS/CNF700, and Pt@CS/CNF900 in half-cells were evaluated through LSV and ADT, respectively (Figure 5a−d). Pt@CS/CNF500, 700, and 900 showed initial mass activities of 366, 300, and 265 mA mg_{Pt}^{-1}, respectively. However, Pt@CS/CNF300 exhibited less activity than the others at the initial LSV as the platinum was not completely reduced and mixed with the aniline. The incomplete reduction of Pt ions was supported by the CV data shown in Figure S16a. H adsorption and desorption were not observed between 0 and 0.2 V vs RHE. Additionally, the broad peak detected around 0.6 V, which represents the electrochemical reduction and oxidation of aniline, indicated that aniline was not decomposed. The CV data also revealed that aniline was not completely carbonized up to 500 °C, with a high and bumpy current density shape in the capacitive current region in Figure S16b. As the ADT cycles proceeded, the platinum ions were electrochemically reduced and exhibited enhanced activity at 10k cycles with Pt@CS/CNF300. Although improved activity was observed at

https://doi.org/10.1021/acsomega.2c00418
ACS Omega 2022, 7, 15615−15624

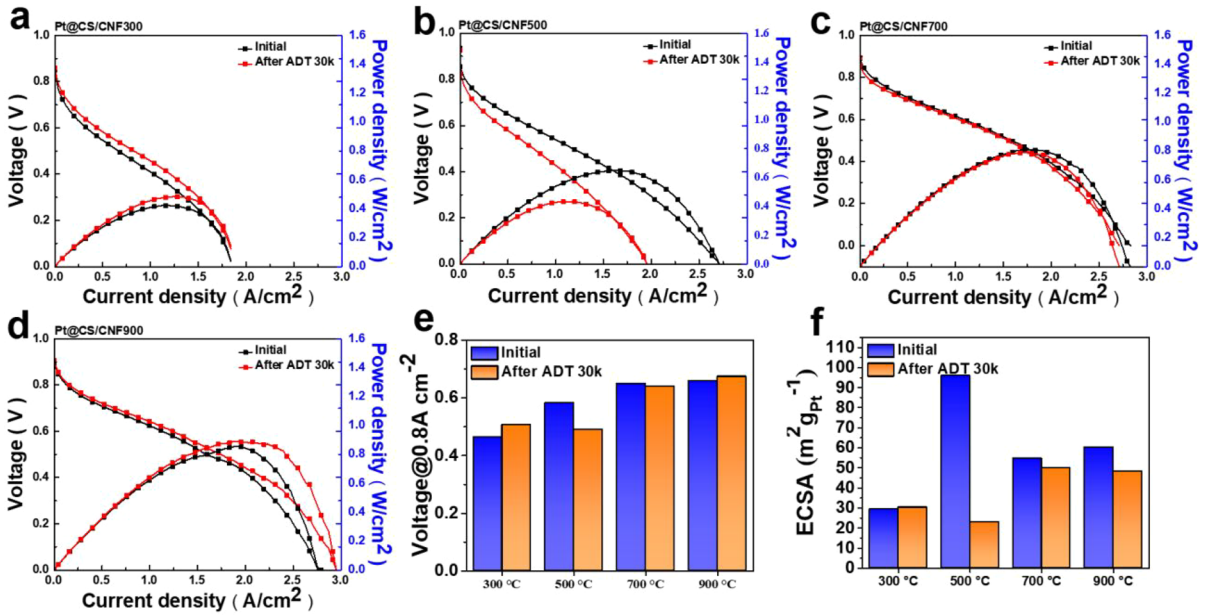

Figure 6. Polarization curves of Pt@CS/CNF (a) 300, (b) 500, (c) 700, and (d) 900. (e) Cell voltages at 0.8 A cm^{-2} and (f) ECSA of Pt@CS/CNF300, 500, 700, and 900 before and after ADT 30k cycles.

10k cycles, it was still relatively lower than that of the initial cycles of the other Pt@CS/CNFs. Additionally, the activity degraded as the ADT continued, and poor activity was observed after 30k cycles. A mass activity loss of 48.9% occurred after ADT as the platinum-covering layer did not act as a protective layer in Pt@CS/CNF300. Pt@CS/CNF500, and Pt@CS/CNF700 also showed mass activity losses of 39.51% and 17.3% after ADT, respectively, while Pt@CS/CNF900 exhibited an improved mass activity of a 16.3% increase (Figure 5e). The hardness of the carbon shell increased with the heat treatment temperature, which is in agreement with the TGA results (Figure 4f); thus, the stability of the catalyst was improved.

The activity and durability of Pt@CS/CNF300, Pt@CS/CNF500, Pt@CS/CNF700, and Pt@CS/CNF900 were also evaluated using unit-cell tests (Figure 6a–d). Pt@CS/CNF300 had the poorest performance, similar to the half-cell test. The initial current densities of Pt@CS/CNF500, Pt@CS/CNF700, and Pt@CS/CNF900 were 0.72, 1.083, and 1.132 A cm^{-2} at 0.6 V. The stability of the catalyst was evaluated by comparing the voltage drop at 0.8 A cm^{-2} before and after ADT. The voltage changes of Pt@CS/CNF300, Pt@CS/CNF500, Pt@CS/CNF700, and Pt@CS/CNF900 were +43, −92, −10, and +15 mV, respectively (Figures 6e and S17). Excluding Pt@CS/CNF300, in which platinum reduction was not completed, the durability of the catalyst with a carbon shell as a protective layer was better than that of a commercial Pt/C catalyst (Figure S18). Heat treatment at a high temperature of 900 °C entirely decomposed the complex and completely carbonized aniline to form a carbon shell with a high degree of graphitization. As ADT proceeds, the carbon shell prevents the dissolution of Pt; thus, the voltage is at 0.8 A cm^{-2} and ECSA maintains its initial value or is slightly reduced.

4. CONCLUSIONS

Three platinum–aniline complexes were characterized to investigate the effect of the complex structure on the activity and stability of platinum catalysts encapsulated by a carbon shell. In the three complexes, the proportion of aniline varied according to the reaction time and preparation process, with different nitrogen to platinum ratios. The higher the nitrogen to platinum ratio, the smaller the nanoparticles that could be obtained by inhibiting their growth during heat treatment. Moreover, due to its higher amount of carbon source in Pt-I than Pt-F or Pt-R, a denser carbon shell was induced; thus, the catalysts synthesized with Pt-I were more durable than the others. To explore the nanoparticle and carbon shell formation process, Pt-I, the most suitable precursor for the platinum core–carbon shell catalyst, was heat-treated at various temperatures. Below 500 °C, Pt-I was not completely decomposed; thus, the oxidation number of the platinum was high and the degree of graphitization of the carbon shell was low due to the chlorine and nitrogen remaining in the composite. Above 600 °C, the carbon shell became robust, and the platinum was converted to a metallic state. As the pyrolysis temperature increased, the activity of the platinum nanoparticles increased along with the stability of the carbon shell. Pt@CS/CNF900 originating from Pt-I exhibited the best performance and durability in the unit-cell test.

■ ASSOCIATED CONTENT

Supporting Information

The Supporting Information is available free of charge at https://pubs.acs.org/doi/10.1021/acsomega.2c00418.

XPS spectra, TGA profile, XRD pattern, and TEM images of Pt–aniline complexes and catalysts synthesized by these Pt–aniline complexes; CV graph of Pt@CS/CNF300,500,700,900 and Pt/C after ADT 30k cycles in half-cell and unit-cell tests (PDF)

■ AUTHOR INFORMATION

Corresponding Authors

Oh Joong Kwon − *Department of Energy and Chemical Engineering, Incheon National University, Incheon 22012, Republic of Korea;* orcid.org/0000-0002-7745-433X; Email: ojkwon@inu.ac.kr

https://doi.org/10.1021/acsomega.2c00418
ACS Omega 2022, 7, 15615−15624

Yong-Hun Cho − *Department of Chemical Engineering, Kangwon Nataional University, Samcheok 25913, Republic of Korea*; Email: yhun00@kangwon.ac.kr

Authors

Jihyeok Song − *Department of Energy and Chemical Engineering, Incheon National University, Incheon 22012, Republic of Korea*

Youngkwang Kim − *Department of Energy and Chemical Engineering, Incheon National University, Incheon 22012, Republic of Korea; School of Chemical and Biological Engineering, Seoul National University, Seoul 08826, Republic of Korea;* orcid.org/0000-0002-1843-366X

Hyo Eun Bae − *Department of Energy and Chemical Engineering, Incheon National University, Incheon 22012, Republic of Korea; School of Chemical and Biological Engineering, Seoul National University, Seoul 08826, Republic of Korea*

Sun Young Kang − *School of Chemical and Biological Engineering, Seoul National University, Seoul 08826, Republic of Korea; Center for Nanoparticle Research, Institute for Basic Science (IBS), Seoul 08826, Republic of Korea*

Jongmin Lee − *School of Chemical and Biological Engineering, Seoul National University, Seoul 08826, Republic of Korea; Center for Nanoparticle Research, Institute for Basic Science (IBS), Seoul 08826, Republic of Korea*

Mohanraju Karuppannan − *Department of Energy and Chemical Engineering, Incheon National University, Incheon 22012, Republic of Korea*

Yung-Eun Sung − *School of Chemical and Biological Engineering, Seoul National University, Seoul 08826, Republic of Korea; Center for Nanoparticle Research, Institute for Basic Science (IBS), Seoul 08826, Republic of Korea;* orcid.org/0000-0002-1563-8328

Complete contact information is available at: https://pubs.acs.org/10.1021/acsomega.2c00418

Author Contributions

‖J.S. and Y.K. contributed equally to this work.

Notes

The authors declare no competing financial interest.

■ ACKNOWLEDGMENTS

This work was supported by the Research Assistance Program (2019) in Incheon National University. Y.-H. Cho acknowledges financial support from the Basic Science Research Program (2019R1D1A3A03103611) through the National Research Foundation of Korea (NRF).

■ REFERENCES

(1) Meier, J. C.; Galeano, C.; Katsounaros, I.; Witte, J.; Bongard, H. J.; Topalov, A. A.; Baldizzone, C.; Mezzavilla, S.; Schüth, F.; Mayrhofer, K. J. J. Design Criteria for Stable Pt/C Fuel Cell Catalysts. *Beilstein J. Nanotechnol.* **2014**, *5* (1), 44−67.

(2) Debe, M. K. Electrocatalyst Approaches and Challenges for Automotive Fuel Cells. *Nature* **2012**, *486* (7401), 43−51.

(3) Ramakrishnan, S.; Karuppannan, M.; Vinothkannan, M.; Ramachandran, K.; Kwon, O. J.; Yoo, D. J. Ultrafine Pt Nanoparticles Stabilized by MoS 2 /N-Doped Reduced Graphene Oxide as a Durable Electrocatalyst for Alcohol Oxidation and Oxygen Reduction Reactions. *ACS Appl. Mater. Interfaces* **2019**, *11* (13), 12504−12515.

(4) Xie, S.; Choi, S.; Lu, N.; Roling, L. T.; Herron, J. A.; Zhang, L.; Park, J.; Wang, J.; Kim, M. J.; Xie, Z.; Mavrikakis, M.; Xia, Y. Atomic Layer-by-Layer Deposition of Pt on Pd Nanocubes for Catalysts with Enhanced Activity and Durability toward Oxygen Reduction. *Nano Lett.* **2014**, *14* (6), 3570−3576.

(5) Chen, C.; Kang, Y.; Huo, Z.; Zhu, Z.; Huang, W.; Xin, H. L.; Snyder, J. D.; Li, D.; Herron, J. A.; Mavrikakis, M.; Chi, M.; More, K. L.; Li, Y.; Markovic, N. M.; Somorjai, G. A.; Yang, P.; Stamenkovic, V. R. Highly Crystalline Multimetallic Nanoframes with Three-Dimensional Electrocatalytic Surfaces. *Science (80-.)* **2014**, *343*, 1339−1343.

(6) Yoo, T. Y.; Yoo, J. M.; Sinha, A. K.; Bootharaju, M. S.; Jung, E.; Lee, H. S.; Lee, B. H.; Kim, J.; Antink, W. H.; Kim, Y. M.; Lee, J.; Lee, E.; Lee, D. W.; Cho, S. P.; Yoo, S. J.; Sung, Y. E.; Hyeon, T. Direct Synthesis of Intermetallic Platinum-Alloy Nanoparticles Highly Loaded on Carbon Supports for Efficient Electrocatalysis. *J. Am. Chem. Soc.* **2020**, *142* (33), 14190−14200.

(7) Gasteiger, H. A.; Kocha, S. S.; Sompalli, B.; Wagner, F. T. Activity Benchmarks and Requirements for Pt, Pt-Alloy, and Non-Pt Oxygen Reduction Catalysts for PEMFCs. *Appl. Catal. B Environ.* **2005**, *56* (1-2), 9−35.

(8) Lee, H.; Sung, Y. E.; Choi, I.; Lim, T.; Kwon, O. J. Novel Synthesis of Highly Durable and Active Pt Catalyst Encapsulated in Nitrogen Containing Carbon for Polymer Electrolyte Membrane Fuel Cell. *J. Power Sources* **2017**, *362*, 228−235.

(9) Chung, D. Y.; Yoo, J. M.; Sung, Y. E. Highly Durable and Active Pt-Based Nanoscale Design for Fuel-Cell Oxygen-Reduction Electrocatalysts. *Adv. Mater.* **2018**, *30* (42), 1704123.

(10) Shao, M.; Chang, Q.; Dodelet, J. P.; Chenitz, R. Recent Advances in Electrocatalysts for Oxygen Reduction Reaction. *Chem. Rev.* **2016**, *116* (6), 3594−3657.

(11) Bing, Y.; Liu, H.; Zhang, L.; Ghosh, D.; Zhang, J. Nanostructured Pt-Alloy Electrocatalysts for PEM Fuel Cell Oxygen Reduction Reaction. *Chem. Soc. Rev.* **2010**, *39* (6), 2184−2202.

(12) Mani, P.; Srivastava, R.; Strasser, P. Dealloyed Binary PtM3 (M = Cu, Co, Ni) and Ternary PtNi 3M (M = Cu, Co, Fe, Cr) Electrocatalysts for the Oxygen Reduction Reaction: Performance in Polymer Electrolyte Membrane Fuel Cells. *J. Power Sources* **2011**, *196* (2), 666−673.

(13) Tian, X.; Luo, J.; Nan, H.; Zou, H.; Chen, R.; Shu, T.; Li, X.; Li, Y.; Song, H.; Liao, S.; Adzic, R. R. Transition Metal Nitride Coated with Atomic Layers of Pt as a Low-Cost, Highly Stable Electrocatalyst for the Oxygen Reduction Reaction. *J. Am. Chem. Soc.* **2016**, *138* (5), 1575−1583.

(14) Lim, B.; Jiang, M.; Camargo, P. H. C.; Cho, E. C.; Tao, J.; Lu, X.; Zhu, Y.; Xia, Y. Pd-Pt Bimetallic Nanodendrites with High Activity for Oxygen Reduction. *Science (80-.).* **2009**, *324* (5932), 1302−1305.

(15) Shao-Horn, Y.; Sheng, W. C.; Chen, S.; Ferreira, P. J.; Holby, E. F.; Morgan, D. Instability of Supported Platinum Nanoparticles in Low-Temperature Fuel Cells. *Top. Catal.* **2007**, *46* (3−4), 285−305.

(16) Zhang, S.; Yuan, X. Z.; Hin, J. N. C.; Wang, H.; Friedrich, K. A.; Schulze, M. A Review of Platinum-Based Catalyst Layer Degradation in Proton Exchange Membrane Fuel Cells. *J. Power Sources* **2009**, *194* (2), 588−600.

(17) Wang, Y.; Chen, K. S.; Mishler, J.; Cho, S. C.; Adroher, X. C. A Review of Polymer Electrolyte Membrane Fuel Cells: Technology, Applications, and Needs on Fundamental Research. *Appl. Energy* **2011**, *88* (4), 981−1007.

(18) Karuppannan, M.; Kim, Y.; Gok, S.; Lee, E.; Hwang, J. Y.; Jang, J. H.; Cho, Y. H.; Lim, T.; Sung, Y. E.; Kwon, O. J. A Highly Durable Carbon-Nanofiber-Supported Pt-C Core-Shell Cathode Catalyst for Ultra-Low Pt Loading Proton Exchange Membrane Fuel Cells: Facile Carbon Encapsulation. *Energy Environ. Sci.* **2019**, *12* (9), 2820−2829.

(19) Kim, Y.; Jeffery, A. A.; Min, J.; Jung, N. Modulating Catalytic Activity and Durability of PtFe Alloy Catalysts for Oxygen Reduction Reaction through Controlled Carbon Shell Formation. *Nanomaterials* **2019**, *9* (10), 1491.

(20) Chung, D. Y.; Jun, S. W.; Yoon, G.; Kwon, S. G.; Shin, D. Y.; Seo, P.; Yoo, J. M.; Shin, H.; Chung, Y. H.; Kim, H.; Mun, B. S.; Lee, K. S.; Lee, N. S.; Yoo, S. J.; Lim, D. H.; Kang, K.; Sung, Y. E.; Hyeon, T. Highly Durable and Active PtFe Nanocatalyst for Electrochemical

Oxygen Reduction Reaction. *J. Am. Chem. Soc.* **2015**, *137* (49), 15478−15485.
(21) Tong, X.; Zhang, J.; Zhang, G.; Wei, Q.; Chenitz, R.; Claverie, J. P.; Sun, S. Ultrathin Carbon-Coated Pt/Carbon Nanotubes: A Highly Durable Electrocatalyst for Oxygen Reduction. *Chem. Mater.* **2017**, *29* (21), 9579−9587.
(22) Ono, L. K.; Yuan, B.; Heinrich, H.; Cuenya, B. R. Formation and Thermal Stability of Platinum Oxides on Size-Selected Platinum Nanoparticles: Support Effects. *J. Phys. Chem. C* **2010**, *114* (50), 22119−22133.
(23) Nie, Y.; Chen, S.; Ding, W.; Xie, X.; Zhang, Y.; Wei, Z. Pt/C Trapped in Activated Graphitic Carbon Layers as a Highly Durable Electrocatalyst for the Oxygen Reduction Reaction. *Chem. Commun.* **2014**, *50* (97), 15431−15434.
(24) Shao, Y.; Yin, G.; Gao, Y. Understanding and Approaches for the Durability Issues of Pt-Based Catalysts for PEM Fuel Cell. *J. Power Sources* **2007**, *171* (2), 558−566.
(25) de Rogatis, L.; Cargnello, M.; Gombac, V.; Lorenzut, B.; Montini, T.; Fornasiero, P. Embedded Phases: A Way to Active and Stable Catalysts. *ChemSusChem* **2010**, *3* (1), 24−42.
(26) Wu, Z.; Lv, Y.; Xia, Y.; Webley, P. A.; Zhao, D. Ordered Mesoporous Platinum@graphitic Carbon Embedded Nanophase as a Highly Active, Stable, and Methanol-Tolerant Oxygen Reduction Electrocatalyst. *J. Am. Chem. Soc.* **2012**, *134* (4), 2236−2245.
(27) Takenaka, S.; Matsumori, H.; Nakagawa, K.; Matsune, H.; Tanabe, E.; Kishida, M. Improvement in the Durability of Pt Electrocatalysts by Coverage with Silica Layers. *J. Phys. Chem. C* **2007**, *111* (42), 15133−15136.
(28) Du, X. X.; He, Y.; Wang, X. X.; Wang, J. N. Fine-Grained and Fully Ordered Intermetallic PtFe Catalysts with Largely Enhanced Catalytic Activity and Durability. *Energy Environ. Sci.* **2016**, *9* (8), 2623−2632.
(29) Wu, G.; More, K. L.; Johnston, C. M.; Zelenay, P. High-Performance Electrocatalysts for Oxygen Reduction Derived from Polyaniline, Iron, and Cobalt. *Science (80-.).* **2011**, *332* (6028), 443−447.
(30) Guo, L.; Jiang, W. J.; Zhang, Y.; Hu, J. S.; Wei, Z. D.; Wan, L. J. Embedding Pt Nanocrystals in N-Doped Porous Carbon/Carbon Nanotubes toward Highly Stable Electrocatalysts for the Oxygen Reduction Reaction. *ACS Catal.* **2015**, *5* (5), 2903−2909.
(31) Jiang, Z. Z.; Wang, Z. B.; Chu, Y. Y.; Gu, D. M.; Yin, G. P. Ultrahigh Stable Carbon Riveted Pt/TiO2-C Catalyst Prepared by in Situ Carbonized Glucose for Proton Exchange Membrane Fuel Cell. *Energy Environ. Sci.* **2011**, *4* (3), 728−735.
(32) Jiang, Z. Z.; Wang, Z. B.; Gu, D. M.; Smotkin, E. S. Carbon Riveted Pt/C Catalyst with High Stability Prepared by in Situ Carbonized Glucose. *Chem. Commun.* **2010**, *46* (37), 6998−7000.
(33) Mohanraju, K.; Lee, H.; Kwon, O. J. High Loading Pt Core/Carbon Shell Derived from Platinum-Aniline Complex for Direct Methanol Fuel Cell Application. *Electroanalysis* **2018**, *30* (8), 1604−1609.
(34) Jiang, Z. Z.; Wang, Z. B.; Chu, Y. Y.; Gu, D. M.; Yin, G. P. Carbon Riveted Microcapsule Pt/MWCNTs-TiO2 Catalyst Prepared by in Situ Carbonized Glucose with Ultrahigh Stability for Proton Exchange Membrane Fuel Cell. *Energy Environ. Sci.* **2011**, *4* (7), 2558−2566.
(35) Cheng, N.; Banis, M. N.; Liu, J.; Riese, A.; Li, X.; Li, R.; Ye, S.; Knights, S.; Sun, X. Extremely Stable Platinum Nanoparticles Encapsulated in a Zirconia Nanocage by Area-Selective Atomic Layer Deposition for the Oxygen Reduction Reaction. *Adv. Mater.* **2015**, *27* (2), 277−281.
(36) Galeano, C.; Meier, J. C.; Peinecke, V.; Bongard, H.; Katsounaros, I.; Topalov, A. A.; Lu, A.; Mayrhofer, K. J. J.; Schüth, F. Toward Highly Stable Electrocatalysts via Nanoparticle Pore Confinement. *J. Am. Chem. Soc.* **2012**, *134* (50), 20457−20465.
(37) Lee, D.; Gok, S.; Kim, Y.; Sung, Y. E.; Lee, E.; Jang, J. H.; Hwang, J. Y.; Kwon, O. J.; Lim, T. Methanol Tolerant Pt-C Core-Shell Cathode Catalyst for Direct Methanol Fuel Cells. *ACS Appl. Mater. Interfaces* **2020**, *12* (40), 44588−44596.
(38) Chen, S.; Wei, Z.; Qi, X.; Dong, L.; Guo, Y.-G.; Wan, L.; Shao, Z.; Li, L. Nanostructured Polyaniline-Decorated Pt/C@PANI Core−Shell Catalyst with Enhanced Durability and Activity. *J. Am. Chem. Soc.* **2012**, *134*, 13252−13255.
(39) Cheng, K.; Kou, Z.; Zhang, J.; Jiang, M.; Wu, H.; Hu, L.; Yang, X.; Pan, M.; Mu, S. Ultrathin Carbon Layer Stabilized Metal Catalysts towards Oxygen Reduction. *J. Mater. Chem. A* **2015**, *3* (26), 14007−14014.
(40) Wen, Z.; Liu, J.; Li, J. Core/Shell Pt/C Nanoparticles Embedded in Mesoporous Carbon as a Methanol-Tolerant Cathode Catalyst in Direct Methanol Fuel Cells. *Adv. Mater.* **2008**, *20* (4), 743−747.
(41) Du, N.; Wang, C.; Long, R.; Xiong, Y. N-Doped Carbon-Stabilized PtCo Nanoparticles Derived from Pt@ZIF-67: Highly Active and Durable Catalysts for Oxygen Reduction Reaction. *Nano Res.* **2017**, *10* (9), 3228−3237.
(42) Ying, J.; Li, J.; Jiang, G.; Cano, Z. P.; Ma, Z.; Zhong, C.; Su, D.; Chen, Z. Metal-Organic Frameworks Derived Platinum-Cobalt Bimetallic Nanoparticles in Nitrogen-Doped Hollow Porous Carbon Capsules as a Highly Active and Durable Catalyst for Oxygen Reduction Reaction. *Appl. Catal. B Environ.* **2018**, *225*, 496−503.
(43) Choi, C. H.; Kwon, H. C.; Yook, S.; Shin, H.; Kim, H.; Choi, M. Hydrogen Peroxide Synthesis via Enhanced Two-Electron Oxygen Reduction Pathway on Carbon-Coated Pt Surface. *J. Phys. Chem. C* **2014**, *118* (51), 30063−30070.
(44) Kralj, S.; Longobardo, F.; Iglesias, D.; Bevilacqua, M.; Tavagnacco, C.; Criado, A.; Delgado Jaen, J. J.; Makovec, D.; Marchesan, S.; Melchionna, M.; Prato, M.; Fornasiero, P. Ex-Solution Synthesis of Sub-5-Nm FeOx Nanoparticles on Mesoporous Hollow N,O-Doped Carbon Nanoshells for Electrocatalytic Oxygen Reduction. *ACS Appl. Nano Mater.* **2019**, *2* (10), 6092−6097.
(45) Geng, L.; Gong, J.; Qiao, G.; Ye, S.; Zheng, J.; Zhang, N.; Chen, B. Effect of Metal Precursors on the Performance of Pt/SAPO-11 Catalysts for n-Dodecane Hydroisomerization. *ACS Omega* **2019**, *4* (7), 12598−12605.
(46) Sahu, N. K.; Prakash, A.; Bahadur, D. Role of Different Platinum Precursors on the Formation and Reaction Mechanism of FePt Nanoparticles and Their Electrocatalytic Performance towards Methanol Oxidation. *Dalt. Trans.* **2014**, *43* (12), 4892−4900.
(47) Wang, S.; Zhang, Y.; Abidi, N.; Cabrales, L. Wettability and Surface Free Energy of Graphene Films. *Langmuir* **2009**, *25* (18), 11078−11081.
(48) Tran, R.; Xu, Z.; Radhakrishnan, B.; Winston, D.; Sun, W.; Persson, K. A.; Ong, S. P. Surface Energies of Elemental Crystals. *Sci Data* **2016**, *3* (1), 160080.
(49) De Toro, J. A.; Vasilakaki, M.; Lee, S. S.; Andersson, M. S.; Normile, P. S.; Yaacoub, N.; Murray, P.; Sánchez, E. H.; Muñiz, P.; Peddis, D.; Mathieu, R.; Liu, K.; Geshev, J.; Trohidou, K. N.; Nogués, J. Remanence Plots as a Probe of Spin Disorder in Magnetic Nanoparticles. *Chem. Mater.* **2017**, *29* (19), 8258−8268.
(50) Ye, S.; Luo, F.; Zhang, Q.; Zhang, P.; Xu, T.; Wang, Q.; He, D.; Guo, L.; Zhang, Y.; He, C.; Ouyang, X.; Gu, M.; Liu, J.; Sun, X. Highly Stable Single Pt Atomic Sites Anchored on Aniline-Stacked Graphene for Hydrogen Evolution Reaction. *Energy Environ. Sci.* **2019**, *12* (3), 1000−1007.

https://doi.org/10.1021/acsomega.2c00418
ACS Omega 2022, 7, 15615−15624